



Cite this: *Nanoscale*, 2020, **12**, 1894

An ovarian spheroid based tumor model that represents vascularized tumors and enables the investigation of nanomedicine therapeutics†

Manu Smriti Singh,^{a,b,c,d,e} Meir Goldsmith,^{a,b,c,d,e} Kavita Thakur,^{f,g}
 Sushmita Chatterjee,^{a,b,c,d,e} Dalit Landesman-Milo,^{a,b,c,d,e} Tally Levy,^{a,b,c,d,e,g,h}
 Leoni A. Kunz-Schughart,^{i,j} Yechezkel Barenholz^k and Dan Peer^l  ^{*a,b,c,d,e}

The failure of cancer therapies in clinical settings is often attributed to the lack of a relevant tumor model and pathological heterogeneity across tumor types in the clinic. The objective of this study was to develop a robust *in vivo* tumor model that better represents clinical tumors for the evaluation of anti-cancer therapies. We successfully developed a simple mouse tumor model based on 3D cell culture by injecting a single spheroid and compared it to a tumor model routinely used by injecting cell suspension from 2D monolayer cell culture. We further characterized both tumors with cellular markers for the presence of myofibroblasts, pericytes, endothelial cells and extracellular matrix to understand the role of the tumor microenvironment. We further investigated the effect of chemotherapy (doxorubicin), nanomedicine (Doxil®), biological therapy (Avastin®) and their combination. Our results showed that the substantial blood vasculature in the 3D spheroid model enhances the delivery of Doxil® by 2.5-fold as compared to the 2D model. Taken together, our data suggest that the 3D tumors created by simple subcutaneous spheroid injection represents a robust and more vascular murine tumor model which is a clinically relevant platform to test anti-cancer therapy in solid tumors.

Received 9th November 2019,
 Accepted 18th December 2019

DOI: 10.1039/c9nr09572a

rsc.li/nanoscale

Introduction

Of all cancer-related mortality, only 10% is caused by primary tumors while the rest of approximately 90% is attributed to metastasis.^{1,2} Ovarian cancer is a lethal gynecological malignancy that is diagnosed in the advanced stage. One-third of all cases are associated with the formation of malignant ascites due to shedding of multicellular clusters from the ovary into the peritoneal cavity.³ Each such cluster (also referred to as a spheroid) holds the potential to initiate tumor formation from the metastatic lesion around the abdominal organs and eventually lead to patient's death.⁴

Growing mini tumors *ex vivo* as spheroids or tumoroids in 3-dimensional (3D) culture for testing the role of hypoxia, drug resistance and drug screening^{2,5} has been in practice for several decades now.^{6,7} *In vitro* spheroids developed from 31 epithelial ovarian cancer cell lines showed stronger molecular and histological similarity to primary tumors than cells grown as monolayers (2-dimensional, 2D).⁴ Most studies which demonstrated the *in vitro* spheroid forming ability of either cancer stem-like cells sorted from the total population of ovarian cancer cell lines⁸ or patient primary tumors⁹ involved the injection of single cell suspension for *in vivo* tumorigenicity assays (minimum cell number to generate a tumor).

^aLaboratory of Precision NanoMedicine, Tel Aviv University, Tel Aviv 69978, Israel.
 E-mail: peer@tauex.tau.ac.il

^bSchool of Molecular Cell Biology & Biotechnology, George S. Wise Faculty of Life Sciences, Tel Aviv University, Tel Aviv 69978, Israel

^cDepartment of Materials Sciences & Engineering, Iby and Aladar Fleiselman Faculty of Engineering, Tel Aviv University, Tel Aviv 69978, Israel

^dCenter for Nanoscience and Nanotechnology, and Tel Aviv University, Tel Aviv 69978, Israel

^eCancer Biology Research Center, Tel Aviv University, Tel Aviv 69978, Israel

^fDepartment of Pathology, Tel Aviv Sourasky Medical Center, Tel Aviv 62431, Israel

^gSackler Faculty of Medicine, Tel Aviv University, Tel Aviv 69978, Israel

^hGynecologic Oncology Unit, Department of Obstetrics and Gynecology, E. Wolfson Medical Center, Holon, Israel

ⁱOncoRay – National Center for Radiation Research in Oncology, Faculty of Medicine and University Hospital Carl Gustav Carus, Technische Universität Dresden and Helmholtz-Zentrum Dresden-Rossendorf, Fetscherstr. 74, 01307 Dresden, Germany

^jNational Center for Tumor Disease (NCT), Partner Site Dresden, Fetscherstr. 74, 01307 Dresden, Germany

^kLaboratory of Membrane and Liposome Research, Department of Biochemistry and Molecular Biology, Institute for Medical Research Israel-Canada (IMRIC), The Hebrew University-Hadassah Medical School, Jerusalem, Israel

[†]Electronic supplementary information (ESI) available. See DOI: 10.1039/c9nr09572a

The lack of clinically relevant animal models to test nanomedicine therapies is cited as one of the major reasons for the failure in clinical trials.^{10–12} The underlying reasons have been partly attributed to heterogeneity in tumor features (proliferation rate and extent of necrosis), vasculature (density and permeability) and stroma (matrix rigidity and architecture).¹¹ With respect to the existing animal tumor models, both syngeneic and xenograft models involve injecting millions of cells that grow at an unnatural pace to form tumors quickly and have a homogeneous cancer cell population.¹⁰ In contrast, a genetically engineered mouse model (GEMM) mimics the *de novo* generation of naturally formed tumors in coordination with the host's non-cancer cells and displays superior correlation to a human clinical setting when compared to other tumor models. However, as these tumors are generated spontaneously and their growth period is not consistent, the response to cancer therapy yields mixed results due to the different stages of disease presentation across the cohort.¹³ This lack of robustness of the model itself limits the usage of a GEMM in routine drug screening *in vivo*.

In contrast, the 3D model mimics a mini-tumor with preformed gradients and represents a tumor mass, which has both proliferating cells at the surface and non-proliferating hypoxic cells at the core⁶ that are most difficult to kill with chemotherapy.¹⁴ Consequently, in this work we evaluated whether: (1) spheroid implantation can form robust *in vivo* tumors and (2) a spheroid-tumor model can be used to test the effectiveness of different types of therapeutics.

Previous studies have shown a correlation between liposome accumulation relative to higher micro-vessel density in the treatment of head and neck cancer and non-small-cell lung cancer.¹⁵ Furthermore, variation in the tumor vascularization within the same type of tumor (*e.g.* colorectal cancer) can also lead to different therapeutic responses across patients. In this context, testing nanomedicine on a 3D tumor model can also be insightful; therefore, we studied and compared the performance of the first approved nanomedicine drug Doxil®¹⁶ on both 3D and 2D tumor models in parallel. Our data suggest that the 3D model represents an alternative and clinically relevant vascularized tumor to test anti-cancer therapeutics.

Results and discussion

Comparable morphology of spheroids from malignant ascites of patients and mice

The ascitic fluid from ovarian cancer patients was assessed immediately after harvesting (Fig. 1A). The spheroid ranged from 50 μm to 450 μm in diameter. The mouse model of intraperitoneal ovarian cancer also led to the formation of ascites in advanced stages (Fig. 1B, representative single spheroid), similar to the spheroid formation in the patient ascitic fluid.

As not all cell lines naturally form spheroids, we first screened the spheroid formation ability of different ovarian cancer cell lines (Fig. S1†). NAR and Ovar8 were selected as they formed intact, robust, and reproducible (NAR – 391 \pm

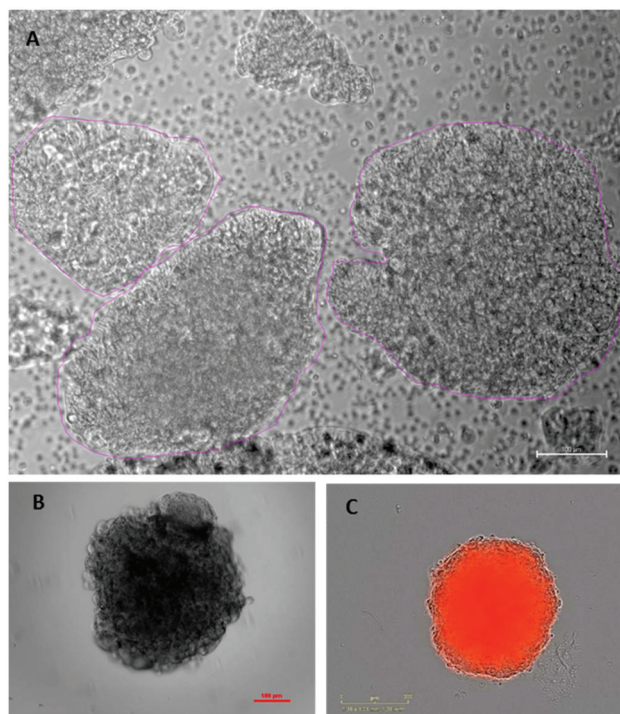


Fig. 1 Comparable morphology between the malignant spheroid from (A) the patient or (B) mice ascites and *in vitro* formed MCTS. (A) Microscopy image of ascites from the ovarian cancer patient shows the presence of an intact spheroid ranging approximately 250–450 μm in diameter (scale bar: 100 μm). (B) A single spheroid from mice ascites (50 days after tumor implantation with 5 million NAR cells) (scale bar: 100 μm). (C). mCherry-labelled NAR cells grown in a 96-well ultra-low attachment (ULA) plate form robust and homogeneous spheroids. A single representative spheroid is shown – 391 \pm 20 μm [day 4] (n = 12) (scale bar: 300 μm), imaged using InCuCyte® (Essen Biosciences).

20 μm and Ovar8 – 356 \pm 8 μm ; n = 12) *in vitro* spheroids (Fig. 1C, representative single spheroid) and were used for further *in vivo* investigation, in which each spheroid would represent a single tumorigenic unit. It is important to note that we tested the spheroid-forming ability from the patient's ascites (data not shown). However, the heterogeneity of the cancer cell population in the patient's sample led to non-reproducible spheroid formation and spheroid size in each experiment. Hence, we decided to use cell lines for further experiments *in vivo*, which are more homogeneous for effective drug screening.

Subcutaneous injection of 3D spheroids leads to robust tumor formation in nude mice

We next evaluated whether a single spheroid injection can lead to the formation of reproducible subcutaneous tumors as a mouse xenograft model. For spheroid formation, cells were seeded at a density of 2000 cells per well on day 0 in an ultra-low attachment 96-well plate. On day 4, the spheroid formation was confirmed under a light microscope (Fig. 1C) and the 96-well plate was taken to the animal house at 4 °C. A single spheroid from each well was injected per mouse. Spheroids

were embedded in media and Matrigel™ (1:1), injected subcutaneously into BALB/c nude mice (Fig. 2A) and monitored for the mCherry signal using the IVIS Spectrum® on day 14 to confirm implantation. The tumors were, however, palpable only at day 40 onwards. Single tumors were formed (Fig. 2B) with both Ovar8 and NAR derived spheroids. We observed that NAR spheroids formed tumors in a robust, consistent (homogeneous in size) and reproducible manner. NAR-based spheroids were used for the rest of our experiments. 20% of mice either did not form tumors or remained dormant for long periods before forming tumors.

Epithelial ovarian cancer cell lines grown *in vitro* as 3D cell culture proliferate slowly and show more chemo-resistance than their 2D monolayer counterparts.⁴ This can possibly explain the slow growth rate of 3D tumors in mice. The progression rate of tumors in animal models is very rapid (in some cases reaching 5 mm in 2 weeks or less) while a relative tumor volume in patients could take years to develop. Most mice models involve injection of millions of cells, wherein most cells die, generating a tumor with necrotic islets and chaotically grown blood vessels. Thus, the current xenografted mice models do not recapitulate the dynamics of spontaneous cancer.

Hence, in parallel, we developed a single-cell suspension-based 2D model to follow the same kinetics as 3D spheroids, which exhibited slow tumor growth. Three different cell den-

sities (5×10^3 , 5×10^4 and 5×10^5) of NAR cells (media and Matrigel™ (1:1)) were injected subcutaneously into different groups of mice and evaluated with respect to tumor volume and necrosis (Fig. S2A†). Each group of mice showed a large standard deviation of tumor volume. The H&E staining of tumor sections (Fig. S2B–D†) of 2D tumors excised after 2 months showed a correlation between the necrotic area and the number of cells injected. Overall, injection of 5×10^5 cells formed big tumors very quickly ($187.1 \pm 119.9 \text{ mm}^3$ on day 65) with a large necrotic core, while injection of 5×10^3 cells showed large standard deviations across tumors ($71.34 \pm 30.7 \text{ mm}^3$ on day 65). The growth rate of 2D tumors formed by the injection of 5×10^4 cells ($96.8 \pm 40.7 \text{ mm}^3$ on day 65) was most comparable with that of a spheroid-based 3D tumor ($84.97 \pm 16.7 \text{ mm}^3$ on day 65). On this basis, 5×10^4 NAR cells were used for injection in the subsequent experiments for the 2D tumor model.

Growth of the 3D spheroid tumor model supported by extensive fibrovascular septa and numerous functional blood vessels

In order to evaluate the pathology of the 2D and 3D tumors with respect to the role of the tumor microenvironment, tumor tissues were excised carefully from the mice and stained with H&E and IHC markers of endothelial cells and myofibroblasts. H&E staining of the whole tumor sections (Fig. 3) shows slow radial growth of 3D spheroids *in vivo* as one tumor unit with more proliferative tumor cells in the periphery and necrosis mostly in the centre (Fig. 3A). In contrast, the 2D model grew as few scattered clusters (island pattern) with less blood vessels and more necrosis seen throughout the tumor sections (Fig. 3B). The number of proliferative cells that stained positive for Ki67+ was higher in the 3D tumor model (Fig. 3C) than in the 2D tumors (Fig. 3D). The 3D tumors grew in an organized fashion with more endothelial cells (CD31+; Fig. 4E and F), myofibroblasts (α SMA+; Fig. 4A and B), and extracellular matrix (Sirius Red staining for collagen; Fig. 3E, superimposed H&E image for Fig. 3G). Fibrovascular septa were present throughout the 3D tumor, which appear as small islets of tumor cells supported by blood vessels and surrounded by myofibroblasts. The 2D tumor model, on the other hand, exhibited fewer numbers of blood vessels (Fig. 4F and H) and thinly distributed collagen deposition (Sirius Red, Fig. 3F and H) due to a scant number of myofibroblasts (Fig. 4B and D).

The difference in the *in vivo* tumor microenvironment observed by pathological analysis of the two models (Fig. 3) was further verified by quantitative PCR expression of different genes involved in stroma–tumor cross-talk (FAP α , NG2), hypoxia (HIF1 α) and angiogenesis (MMP9, CD31) (Fig. 4I). The expression of NG2, a marker for perivascular pericytes, was higher in 3D tissues than in 2D tumor tissues. Since extensive endothelial cell staining was observed in 3D tissues (Fig. 4E and G), CD31 expression was quantified by RT-PCR and correlated well. Myofibroblasts are absent in the normal ovary tissue but have marked presence in the epithelial ovarian cancer tissue.¹⁷ Higher expression of FAP α in RT-PCR corre-

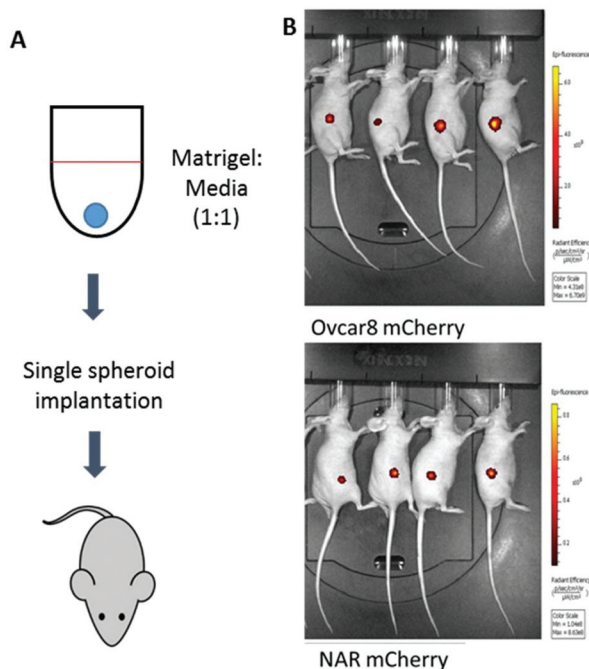


Fig. 2 *In vivo* spheroid implantation in mice. (A) A total volume of 150 μ L Matrigel media (1:1) encasing a single spheroid is picked from each well (of an ultra-low attachment 96-well plate) using a 21G syringe and injected subcutaneously into the mice on the right flank. (B) Mice injected with mCherry labelled-Ovar8 or -NAR spheroids 48 days post spheroid implantation were monitored using the *In Vivo* Imaging System (IVIS, PerkinElmer).

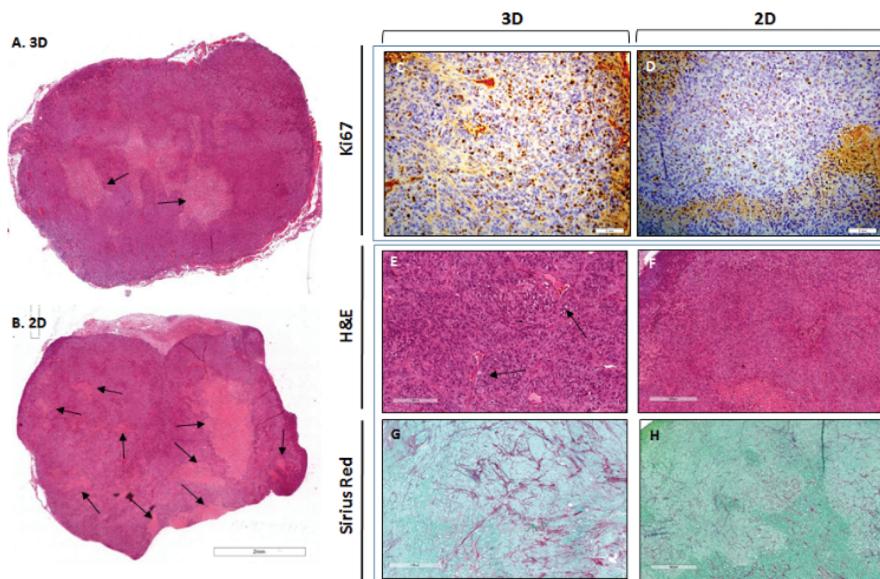


Fig. 3 Histopathology of tumor models: Cross-sections of 3D (A) and 2D (B) tumor samples on day 90 [scale bar: 2 mm]. 3D tumors show less necrosis predominantly in the centre (arrows) as compared to patchy necrosis throughout the 2D tumor tissue. In 3D tumors, Ki67 positive mitotic cells showed stronger immunostaining and are mostly present in the periphery of spheroid-derived tumors, (C) whereas in the 2D model, Ki 67 positive cells showed weaker staining. (D) The presence of collagen fibres was evaluated with Sirius Red staining in 3D (G) and 2D (H) tumor sections. The spheroid-derived tissue (G) shows cancer cell growth supported by an extensive extracellular matrix; the superimposed H&E section (E) shows the deposition of fibres around blood vessels. The 2D tumor showed less and scattered collagen deposition (H: Sirius Red, F: H&E) [scale bar: A and B: 2 mm; C and D: 100 μ m; and E–H: 400 μ m].

lated with the dense presence of α SMA. Both α SMA and FAP α are myofibroblast markers which are present in abundance in 3D tissues (Fig. 4A and C). High α SMA expression has been shown to correlate with earlier disease recurrence and enhanced tumor aggressiveness in patients with serous ovarian carcinoma.¹⁸

Secretion of HIF1 α from the hypoxic 3D spheroid core possibly attracts both fibroblasts and endothelial cells during the establishment of the tumor niche¹⁹ to mediate tumorigenesis and metastasis.²⁰ This could be the result of the presence of hypoxia in spheroids at the time of implantation in mice. Hence, we evaluated the expression of hypoxia-related genes: carbonic anhydrase 9 (CA9) and HIF1 α in 4 day spheroids as compared to the expression in cells grown in 2D cell culture (Fig. S3 \dagger). The expression of both the genes was 3–10-fold higher in both the cell lines compared to the 3D counterparts, suggesting their role in promoting angiogenesis from the time of implantation in mice. In addition, we performed pimonidazole staining of NAR spheroids (2000 cells per well; 391 \pm 20 μ m on day 4) which indicates severe hypoxia in cells at a pO₂ of 10 mm Hg or lower (around 1.2% oxygen) but does not show severe hypoxia (Fig. S4A \dagger) under routine culture conditions. However, exposure of spheroids for 6 (Fig. S4B \dagger) and 24 h (Fig. S4C \dagger) to tissue normoxic conditions (8% O₂), reflecting *in vivo* conditions upon implantation in mice, results in rapid and progressive oxygen deficiency in spheroid cells.

The presence of additional blood vessels in the 3D tumor model could potentially be due to a 4- and 2-fold higher expression of MMP9 and HIF1 α respectively (Fig. 4I). MMP9 is

established to assist in tumor progression and growth by degrading the basement membrane to cleave the membrane bound VEGF from endothelial cells, which further facilitates angiogenesis.²¹ MMP9 up-regulation has also been associated with a decrease in ovarian cancer survival clinically.²¹ As a result of reactive tumor stroma in the 3D model, increased deposition of ECM components or fibrosis²² is evident (Fig. 3G and E). Ovarian cancer is also known to form highly fibrotic tissues with a well-knit ECM, providing support to tumor cells.²³

Overall, we observed that the 3D tumor model developed here from the drug resistant NAR cell line follows a slow proliferation rate and corresponds to a highly dynamic TME formed in clinically resistant tumor types rich in activated fibroblasts and supportive vasculature.

The effect of different classes of cancer therapeutics on the tumor growth rate in 2D and 3D models

Morphologically, spheroid-derived tumors grew as single, visibly round and uniform tumors (Fig. 5E, 3D) compared to the 2D tumors, which in some cases grew as elongated or multiple tumor subsets (Fig. 5E, 2D). In order to evaluate the effect of therapies on the two mice tumor models we chose to work with formulation-free doxorubicin (F-Dox) as a representative chemotherapy; Doxil®, liposomal doxorubicin, as a representative nanomedicine (see the physicochemical characterization in Fig. S4 \dagger) and Avastin® to represent biological therapeutics. The rationale for using F-Dox in this study was based on the prevailing use of Doxil® for the treatment of ovarian cancer²⁴

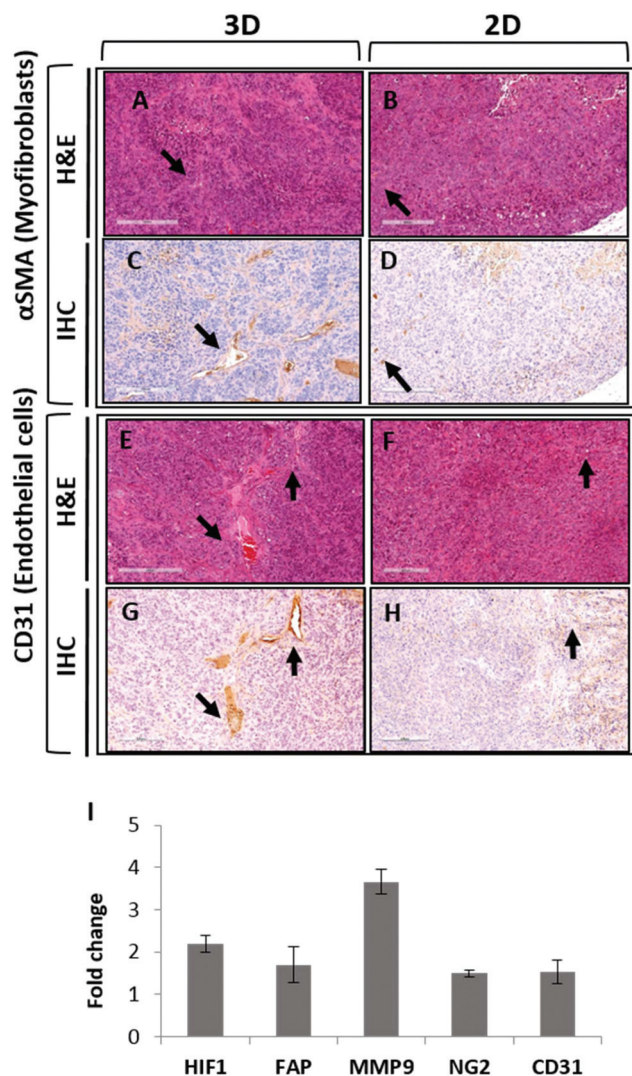


Fig. 4 Stromal components of the tumor microenvironment in the two models: H&E and IHC staining of 3D (A, C, E, G) and 2D (B, D, F, H) tumor sections. (A–D) 3D tumor sections (A, C) having more myofibroblasts than 2D tumor sections (B, D) stained with α SMA; (E–H) endothelial cells stained with CD31; 3D tumor sections (E, G) having more blood vessels than 2D tumor sections (F, H); (I) relative quantification of genes in 3D tumor sections compared to 2D tumor sections. HIF1 α – hypoxia inducible factor 1 α ; FAP α – fibroblasts activated protein (myofibroblast marker); MMP9 – matrix metalloproteinase 9; NG2 – neural/glial antigen-2 (pericyte marker); CD31 – cluster of differentiation 31 (endothelial cell marker); $n = 3$; [scale bar: A–D: 300 μ m; E–H: 200 μ m].

and the ease of quantification of the fluorescent drug.²⁵ The treatments were given alone or in combination as shown in the scheme (Fig. S5[†]). Except for F-Dox, differences in the therapeutic efficacy were observed between 3D (Fig. 5A, 3D) and 2D (Fig. 5B, 2D) models across treatment groups.

Examining the effect of different kinds of therapeutics (Fig. 3) on the growth kinetics of only the 2D model for pre-clinical assessment would lead to a false conclusion: Doxil $\text{\textcircled{R}}$ shows equivalent efficacy to F-Dox. However, the same experiment performed on the 3D model revealed that Doxil $\text{\textcircled{R}}$ is

much more efficacious than F-Dox. We hypothesize that in the 2D model, since the blood vessels are less organized, drug distribution is mostly achieved by passive diffusion through a loose ECM and necrotic area in the tumor mass. However, in the 3D model F-Dox is less effective due to small passive diffusion through a tighter ECM. Doxil $\text{\textcircled{R}}$, on the other hand, shows significantly higher accumulation and anti-tumor efficacy in the 3D tumor model (Fig. 6D) either when administered alone or in combination with Avastin $\text{\textcircled{R}}$, due to a more vascularized tumor structure. Effectively, this shows an accentuated enhanced permeability and retention (EPR) effect in the 3D tumors but not in the 2D tumor models.

Treatment with Avastin $\text{\textcircled{R}}$ alone exhibited low therapeutic effects on the 3D tumor and no effects on the 2D tumor model. On the other hand, in both 3D and 2D models, co-administration of Avastin $\text{\textcircled{R}}$ improved the delivery of both F-Dox and Doxil $\text{\textcircled{R}}$. Interestingly, a similar magnitude of therapeutic benefit was achieved when F-Dox was co-administered with Avastin $\text{\textcircled{R}}$ in both 3D and 2D tumor models leading to reduction in tumor volumes by 2.6- and 2.4-fold respectively, in comparison with the control group.

In the 3D model, treatment with Doxil $\text{\textcircled{R}}$ was highly efficacious (Fig. 5A, 3C) as compared to the treatment of the 2D model (Fig. 5B, 3D). In the 3D model, tumor volumes were significantly reduced when Doxil $\text{\textcircled{R}}$ was administered either alone (\sim 4.8-fold) or in combination with Avastin $\text{\textcircled{R}}$ (\sim 10-fold) as compared to the control group. Nanocarrier delivery to tumors is predominantly a function of blood vessels.^{26–28} The superior therapeutic effect of Doxil $\text{\textcircled{R}}$ in the 3D *in vivo* model as compared to the 2D model could possibly be explained on the basis of the extent of angiogenesis that was further evaluated.

Improved Doxil $\text{\textcircled{R}}$ delivery to 3D tumors owing to the increase in the number of blood vessels

In order to understand the superior therapeutic effects of Doxil $\text{\textcircled{R}}$ in 3D tumors, we evaluated the functionality of blood vessels by co-staining the vessels with endothelial cells and pericytes. Pericytes lining around endothelial cells are responsible for the maturity of blood vessels, making them functional.²⁹ The blood vasculature is markedly aberrant in tumor tissues. This is characterized by high tumor interstitial fluid pressure (IFP), poor perfusion of oxygen, and inadequate coverage of pericytes around the endothelial cells (Fig. 6A, cross-section of normal blood vessels in mouse skin). We found that the few blood vessels that were present in the 2D tumors showed anomalous localization of pericytes around the endothelial cells (Fig. 6B). In contrast, the 3D tumors exhibit the presence of thick pericytes around almost all endothelial cells (Fig. 6C). Large blood vessel lumina were markedly present throughout the 3D tissue as compared to the 2D tumors.

Next, we wanted to evaluate how the presence of blood vessels and pericyte coverage around endothelial cells correlates with doxorubicin delivery (F-Dox or Doxil $\text{\textcircled{R}}$) in both 2D and 3D tumor tissues. 2 hours post intravenous injection, significantly higher accumulation (\sim 2.5-fold) of doxorubicin delivered *via* Doxil $\text{\textcircled{R}}$ was observed in all the 3D tumor samples as

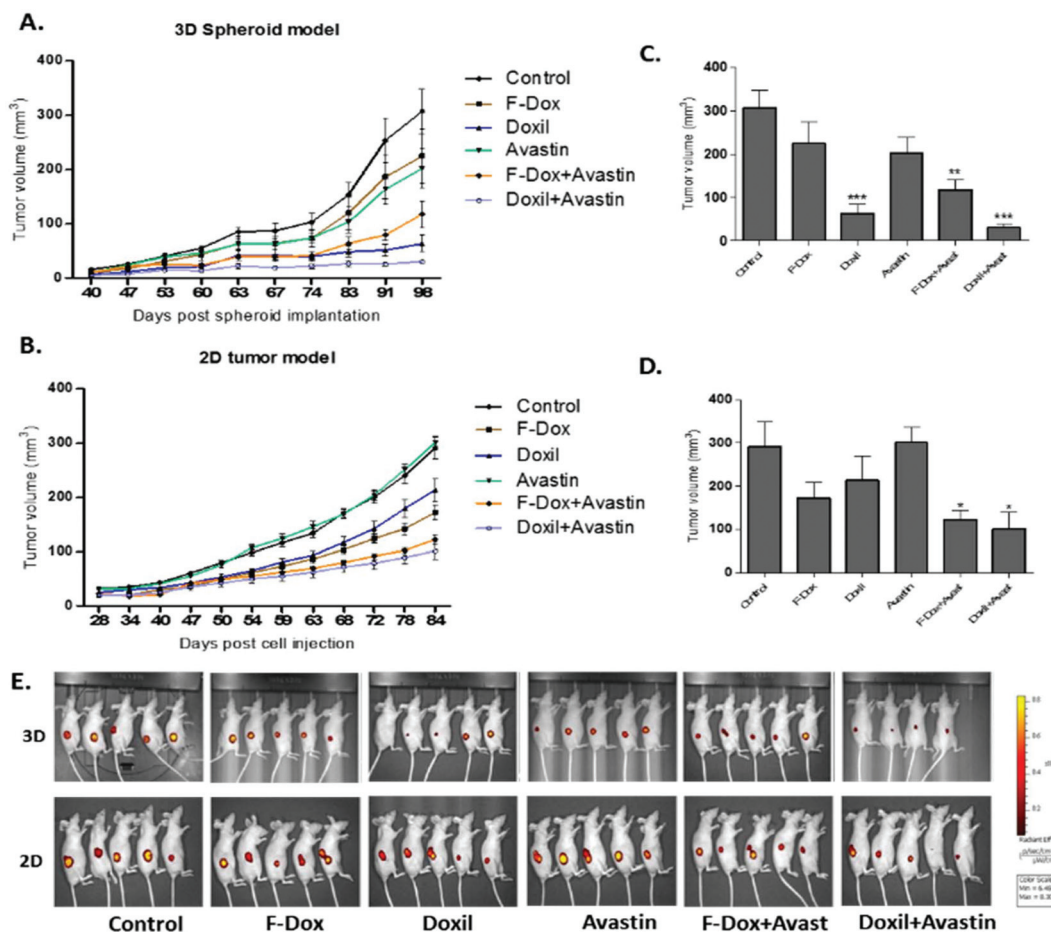


Fig. 5 Growth kinetics of 2D vs. 3D tumors in mice: (A) the 3D spheroid-based tumor and (B) the 2D-based tumor. Mice were administered with F-Dox (5 mg kg⁻¹), Doxil® (5 mg kg⁻¹) or Avastin® (25 mg kg⁻¹) alone or in combination. One-way ANOVA followed by Dunnett's Multiple Comparison Test was performed for treatment *versus* control in (C) 3D tumors and (D) 2D tumors; $p < 0.01$. (E) IVIS images normalized to show the extent and intensity of mCherry tumors *in vivo* for 3D and 2D tumors on day 84.

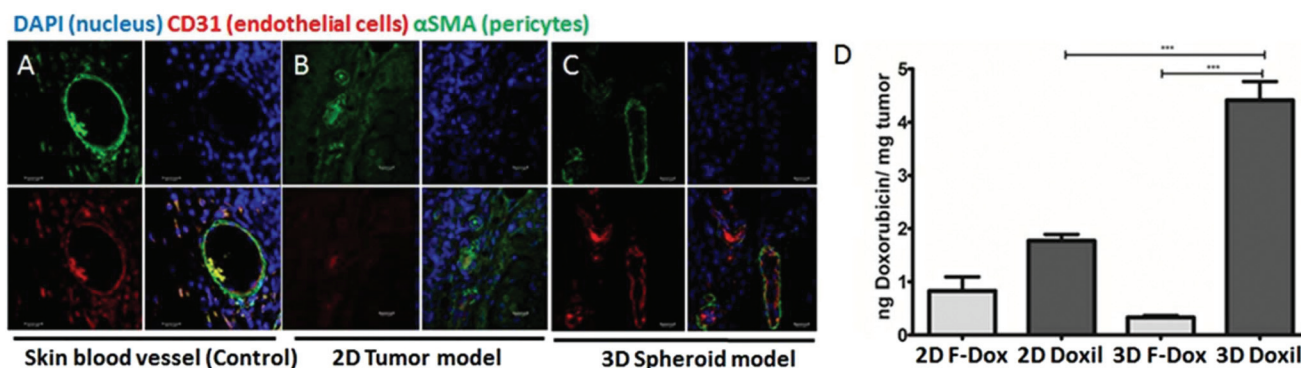


Fig. 6 Assessment of blood vessel functionality and doxorubicin accumulation in tumor models. Blood vessel functionality was evaluated by immunofluorescence staining of: pericytes (αSMA, green), endothelial cells (CD31, red) and nucleus (DAPI, blue) on 90-day tumor sections. The presence of pericytes around endothelial cells indicates functional blood vessels: (A) skin (control), (B) 2D tumor, and (C) 3D spheroid tumor. (D) 3D- and 2D-based tumor bearing mice were injected with an equivalent dose of F-Dox and Doxil®. 1 hour post injection, the mice were sacrificed, and tumors were excised and lysed to extract doxorubicin. Doxorubicin was quantified by spectroscopy. Over 2.5-fold higher accumulation of doxorubicin was observed in 3D tumors when delivered *via* Doxil® (scale bar: 20 μm).

compared to the 2D tumors (Fig. 6D). This might be a strong evidence for the improved therapeutic response of Doxil® in the 3D tumor model as compared to the 2D model. The accumulation of doxorubicin delivered *via* F-Dox was almost negligible in the 3D tumors as compared to the 2D tumors, which might be due to a dense extracellular matrix as shown by the presence of stromal components in the 3D tumor (Fig. 3G).

Our work correlates with pronounced accumulation of doxorubicin delivered *via* Doxil®, which is associated with increased microvessel density in a phase I clinical trial in head and neck and non-small cell lung cancer patients.¹⁵

The synergistic effect of Avastin® can be explained by normalization of blood vessels owing to the blockage of angiogenic signaling.³⁰ This normalization of blood vessels leads to reduced microvessel density (number of vessels per square millimeter) and maturation of nascent vessels through active pericyte recruitment (number of α SMA + vessels per number of blood vessels).³¹ By both these mechanisms, decreased vascular permeability likely ensues, also decreasing the interstitial fluid pressure of the tumor. The normalization of blood vessels in the tumor tissue delivers drugs in more effective ways,^{28,32} explaining the increased delivery of Doxil® to 3D tumors in our work. Furthermore, vascular normalization with Avastin® contributed to enhanced penetration of both F-Dox and Doxil®.

Avastin® co-administration with anti-cancer treatment showed superior therapeutic efficacy than that achieved with either F-Dox or Doxil® administered alone. This can possibly be explained by the previous work of Jain *et al.*³¹ which reported that a therapeutic benefit was observed in breast cancer patients due to Bevacizumab (Avastin®) mediated pruning and normalizing of the pre-existing blood vessels. However, the effect was beneficial only for the breast cancer patient cohort where a sufficient number of blood vessels were already present (in our case – the 3D tumors). However, additional extravasation mechanisms such as transendothelial transport of F-Dox or Doxil® from the luminal to the abluminal side of endothelial cells through the tumor matrix can also explain the enhanced therapeutic effect.³³

Thus, differences in the tumor architecture in terms of the ECM and functional vascular networks can explain drug penetration of F-Dox *versus* Doxil® treatment. This provides insight into why most drugs fail in clinical trials, and hence the need to develop more clinically relevant and robust tumor models.

Conclusions

In this work, we establish a robust tumor model that can be created by simple subcutaneous injection of pre-formed spheroids. On the basis of histopathology, the 3D spheroid model exhibits slower growth, possibly recapitulating the tumor origin. The proliferative zone is organized within a framework of extensive myofibroblasts and endothelial cells forming fibrovascular septa. Hence, the 3D tumor model certainly

shows a greater degree of tumor–stroma interaction as compared to the 2D tumor model. Although 3D *in vitro* cell culture is known for a long time, we further developed the 3D spheroids as an *in vivo* tumor model and employed it to test Doxil® and Avastin® as representatives of anti-cancer therapies. Our results demonstrate that the presence of functional blood vessels is paramount to enhancing the delivery of Doxil® to tumors. This antitumor effect can be further accentuated by modulation of the tumor vasculature with an antiangiogenic agent (Avastin®), which rectifies the structural abnormalities and makes the blood vessels more functional for drug delivery strategies. The existing 2D models enable the study of the interactions between nanocarriers and tumors with little vascularization. The 3D model enables the exploration of how nanocarriers interact with highly vascularised tumors, thus providing a platform to produce more effective nanocarrier-based treatments.

Additional characterization of 3D spheroid tumors and their comparison to clinical tumors would warrant the understanding of drug distribution profiles in phenotypically distinct tumor types.

Experimental section

Materials

96-Well ultra-low attachment plates were purchased from Greiner Bio-one, Frickenhausen, Germany. Doxorubicin and Doxil® were obtained from Teva Pharmaceutical Industries (Israel) and Janssen Pharmaceutica (Belgium) respectively. Avastin® (Roche) was a kind gift from Prof. Ido Wolf, Tel Aviv Sourasky Medical Center. The following antibodies were used: Ki67 (SP6) (275R-14, Cell Marque); alpha Smooth Muscle Actin (NB300-978, Novus Biologicals); and CD31 (250590, Abbiotec). Picro Sirius Red was purchased from Abcam (ab150681). The cDNA Reverse Transcription Kit and the EzRNA purification kit were purchased from Quanta Biosciences and Biological Industries, Beit Haemek, Israel, respectively. The Step one Sequence Detection System and SYBR green were obtained from Applied Biosystems Foster City, CA. For spheroid staining, primary anti-pimonidazole antibody and DAPI were obtained from Hypoxyprobe™-1, hpi Inc and Dako, USA respectively. Secondary fluorescence-labeled antibody (Alexa Fluor 488 goat anti-rabbit) and fluorescent mounting medium were purchased from Invitrogen.

Tumor cell lines and spheroid culture

Monolayers of Ovarc3, Ovarc4, Ovarc8 and NCI/Adriamycin Resistance (NAR) cells were cultured in RPMI-1640 media supplemented with 10% fetal bovine serum, penicillin (100 U mL⁻¹), streptomycin (0.1 mg mL⁻¹) and L-glutamine (2 mM). Following trypsinization and counting, spheroids were generated by seeding different cell densities (500–5000 cells) per well in 200 μ l media (Fig. S1A†) on a 96-well ultra-low attachment, rounded-bottom plate. Formation of spheroids and their growth kinetics were assessed after 96 h until day 13

(Fig. S1B†), using a phase contrast microscope (Eclipse Ti, Nikon, Tokyo, Japan). Ovar8 and NAR were selected for *in vivo* testing.

NAR cells were stably transfected with the pEF1alpha-mCherry-N1 vector (Clontech) using the Lipofectamine 2000 transfection reagent (Invitrogen). The cells were positively selected using 0.5 mg mL⁻¹ G418 24 h after the transfection. Ovar8 cells were stably transduced using the pLL-CMV-mCherry lentivirus. Transduced cells were sorted according to their mCherry expression, and the highest mCherry population was collected.

Ascite collection from a patient and a mouse intraperitoneal ovarian cancer model

Ascites were collected during primary debulking surgery from an ovarian cancer patient with recurrent disease. The study was approved by the Institutional Review Board of the Wolfson Medical Center affiliated to the Sackler School of Medicine, Tel Aviv University and was performed in accordance with the NIH Guidelines. Informed consents were obtained from human participants of this study. All animal protocols were approved by Tel Aviv University's Institutional Animal Care and Use Committee.

Mice were injected with 5 million NAR cells intraperitoneally and monitored routinely to follow weight gain to assess the formation of ascites. On day 50, the mice were sacrificed and the ascitic fluid was harvested from the peritoneal cavity.

Imaging of ascites from both the patient and mice was done using a phase contrast microscope (Eclipse Ti, Nikon, Tokyo, Japan).

Subcutaneous injection of NAR spheroids in mice

Athymic nude female mice (6 weeks old) were purchased from Envigo (Israel). The mice were maintained and treated according to the National Institute of Health guidelines. All animal protocols were approved by the Tel-Aviv Institutional Animal Care and Use Committee. For tumor implantation in the 3D model, 2000 cells were seeded per well in 200 µl media. On day 4, the diameter of spheroids was approximately ~400 µm, and the number of cells in a single spheroid was determined to be in the range of 6500–7200.

Spheroids, syringes, Matrigel™, PBS, and tips were placed in a tissue culture hood and pre-cooled in an ice bucket to maintain a temperature below 4 °C. 125 µl media were removed carefully and 75 µl Matrigel™ was added to each well of the 96-well plate. In a 21G syringe, the dead volume was removed by pre-filling with sterile PBS and then a single spheroid embedded in Matrigel™: the medium (1:1) was injected subcutaneously (S.C.) into the right flank of SCID-nude mice. Each well of the 96-plate was subsequently checked under a light microscope to ensure that the spheroids were picked from each well.

For the development of a 2D model, a single cell preparation of NAR cells was obtained following trypsinization. 5 × 10³, 5 × 10⁴ and 5 × 10⁵ NAR cells (in 150 µl media and Matrigel™ (1:1)) were injected S.C. (Fig. S2†). The 2D model

was set up by choosing an injection of 5 × 10⁴ cells, as the tumors exhibited a lower standard deviation than, comparatively less necrosis than and similar growth kinetics to the 3D model. The tumor volume was measured using an electronic caliber and the tumor volume was calculated using the formula: (length × (width)²)/2.

Treatment and tumor growth kinetics

Implantation of spheroids was confirmed by using the *In Vivo* Imaging System (IVIS) Spectrum (PerkinElmer, Waltham, MA, USA) on day 14 post spheroid injection in mice. Mice from the treated group were administered intravenously with Avastin® (25 mg kg⁻¹), doxorubicin (5 mg kg⁻¹), or Doxil® (5 mg kg⁻¹) alone or in combination once a week for 4 weeks (Fig. S5†).

Quantification of mRNA levels by qPCR

Tumor tissues that developed from the NAR xenografted 2D and 3D models were collected and stored immediately at -80 °C. For RNA extraction, 2 mg of tissue per sample was used, cut into small pieces and homogenized in lysis solution with a handheld homogenizer. RNA was extracted using the EzRNA purification kit. The quality of RNA was checked in denaturing gel and only the samples with good quality of RNA were used in the study. 1 µg of RNA from each sample was reverse transcribed into cDNA using the cDNA Reverse Transcription Kit. A standard curve was plotted using 1–100 ng of cDNA and their respective Ct (threshold cycle) values. 10 ng of cDNA was found to be optimal for evaluating the expression of the genes used in this study. Real-time amplification was performed with the step one Sequence Detection System using SYBR green. The gene expression level in the xenografted 3D tumor tissue as compared to the 2D tumor tissue was analyzed by 2-ΔΔCT method and plotted as a fold change in the graph. The following primer sequences were used for qPCR:

HIF1α Fwd: 5'TTCACCTGAGCCTAATAGTCC3'
 HIF1α Rev: 5'CAAGTCTAAATCTGTGTCCTG3'
 MMP9 Fwd: 5'TTGACAGCGACAAGAAGTGG3'
 MMP9 Rev: 5'GCCATTCACGTCGTCCTTAT3'
 Fapα Fwd: 5'CCAGTTCCAGAAATGATAGCC3'
 Fapα Rev: 5'GACAGGACTGAGACATTCTGC3'
 CD31 Fwd: 5'TACAGTGGACACTACACCTG3'
 CD31 Rev: 5'GACTGGAGGAGAACTCTAAC3'
 NG2 Fwd: 5'CGCTGACCTCCGATGTTTC3'
 NG2 Rev: 5'AAGTTGCCACGCTTGTCC3'
 Col1a Fwd: 5'ACGCATGGCCAAGAAGAC3'
 Col1a Rev: 5'GGTTTCCACGTCTCACCATT3'

Doxil® characterization

Doxil® lipid composition (Fig. S4†) was characterized for phospholipid concentrations by the modified Bartlett method³⁴ and for individual lipid components by high-performance liquid chromatography coupled with evaporative light-scattering detection (ELSD). The size distribution and polydispersity index (PDI) were determined by dynamic light scattering (DLS) using a Malvern Zetasizer Nano ZS instrument (Worcestershire, UK) at an angle of 173°. For this, Doxil

samples were diluted 1 : 50 in sterile saline (0.9% NaCl) and pre-filtered through a 200 nm pore-membrane. The zeta potential was also determined using a Malvern Zetasizer Nano ZS instrument. For zeta potential measurements, Doxil was diluted in 1.5 mM sodium nitrate; drug encapsulation was determined using the cation exchanger Dowex 50 assay.¹⁸ Direct imaging of the liposomes was performed by cryo-TEM as previously described.³⁵

All the acquired images were analyzed using the Vironova Analyzer Software (VAS, Vironova AB, Stockholm, Sweden). Automatic particle picking was performed on the relevant images, followed by a manual curation step, during which falsely detected particles were removed and undetected particles of interest were added. An independent review of the particle detection was performed in order to limit the number of erroneously identified particles.

Histological analysis

On completion of the study, the animals were sacrificed and the tumors were dissected and kept in formalin solution. The tumors were then transferred to ethanol, cut into 5 μm thick sections on an RM2235 microtome (Leica Biosystems) to perform Hematoxylin and Eosin (H&E) or immunohistochemistry (IHC) staining with the following antibodies: Ki67, alpha Smooth Muscle Actin, and CD31. Images were acquired with an Aperio VERSA digital pathology scanner (Leica Biosystems).

Pimonidazole staining of spheroids

2000 or 7000 cells per well were seeded in a 96-well ultralow attachment plate on day 0. Spheroids grown under tissue normoxic conditions were exposed to 8% O₂ using a BioSpa8 incubation system (BioTek). 4-Day spheroids were carefully harvested from the 96-well plates with cut tips and washed twice with PBS. For measurements, serial cryostat sections with a thickness of 5 μm through the center region of spheroids were made. To visualize hypoxia, spheroids were exposed to 20 $\mu\text{g ml}^{-1}$ pimonidazole (green, 1 : 2500) for 2 h at 37 °C before shock-freezing and further processing. Cell nuclei (blue) were counterstained with 1 μM DAPI.

Doxorubicin accumulation in tumors

Doxorubicin was quantified as previously described.²⁵ NAR cell-based tumor bearing mice were randomly divided and were treated when the mean tumor diameter was in the range of 6 to 8 mm. Doxorubicin and Doxil were injected intravenously at a dose equivalent to 5 mg kg⁻¹ to enable quantification of the drug in tissues. The mice were sacrificed 2 hours later, and tumors were excised, weighed and immediately frozen at -80 °C. The tumors were cut into small pieces and homogenized using stainless steel beads (SSB14B) in the Bullet Blender Storm 24 (Next Advance Inc., USA) in acidified isopropanol (81 mM HCl in isopropanol). The fluorescence of doxorubicin was quantified using the a Synergy HT multi-mode microplate reader (BioTek, VT, USA) with an excitation at 490 nm and an emission maximum at 560–590 nm using a standard curve as was previously shown.^{36,37}

Statistical analysis

Statistical analysis was performed using GraphPad Prism 5.03 software (GraphPad Software, San Diego, CA, USA). The results are presented as mean \pm SEM. More than two groups were analyzed using one-way ANOVA followed by the Bonferroni post-test.

Conflicts of interest

Yechezkel Barenholz is one of the inventors on two already expired (March 2010) patents relevant to Doxil: (1) Y. Barenholz and G. Haran, Method of Amphipathic Drug Loading in Liposomes by pH Gradient, U.S. Patent 5192549, 1993. U.S. Patent 5244574, 1993; (2) Y. Barenholz and G. Haran, Liposomes: Efficient Loading and Controlled Release of Amphipathic Molecules, U.S. Patent 5316771, 1994. The Hebrew University received royalties from Doxil sales until the patents expired. The Barenholz Fund was established with part of these royalties, and is used to support Barenholz research.

The rest of the authors do not have any conflicts of interest.

Acknowledgements

The authors thank Dr Dima Shamrakov, Ayana Ltd, Jerusalem Biotechnology Park, Hadassah Ein Kerem Campus, Jerusalem 91120, Israel for the determination of Doxil® composition, size, zeta potential, and VAS analysis of the cryoTEM; and Einat Nativ-Roth of Ilse Katz Institute for Nanoscale Science and Technology, Ben-Gurion University of the Negev, Be'er Sheva 84105, Israel for performing the CryoTEM.

The authors gratefully acknowledge the technical assistance of Marit Wondrak and Lisa Eckhardt at OncoRay, Technical University Dresden.

This work was supported in part by the Israel Science Foundation (ISF) grant # 1178/16, the Rivkin Foundation and the Len and Susan Mark program in Ovarian Cancer awarded to D. P. M. S. S. would like to thank Centre for Nanoscience and Nanotechnology, Tel Aviv University for awarding travel grant as a visiting fellow at OncoRay – Center for Radiation Research in Oncology, Faculty of Medicine, Technical University, Dresden.

We would like to thank Brandon Ng for valuable suggestions on the manuscript.

Notes and references

- 1 C. L. Chaffer and R. A. Weinberg, *Science*, 2011, **331**, 1559–1564.
- 2 T. Rodrigues, B. Kundu, J. Silva-Correia, S. C. Kundu, J. M. Oliveira, R. L. Reis and V. M. Correlo, *Pharmacol. Ther.*, 2018, **184**, 201–211.
- 3 E. Kipps, D. S. Tan and S. B. Kaye, *Nat. Rev. Cancer*, 2013, **13**, 273–282.

- 4 J. M. Lee, P. Mhaweche-Fauceglia, N. Lee, L. C. Parsanian, Y. G. Lin, S. A. Gayther and K. Lawrenson, *Lab. Invest.*, 2013, **93**, 528–542.
- 5 F. Hirschhaeuser, H. Menne, C. Dittfeld, J. West, W. Mueller-Klieser and L. A. Kunz-Schughart, *J. Biotechnol.*, 2010, **148**, 3–15.
- 6 J. Friedrich, C. Seidel, R. Ebner and L. A. Kunz-Schughart, *Nat. Protoc.*, 2009, **4**, 309–324.
- 7 A. Riedl, M. Schleder, K. Pudelko, M. Stadler, S. Walter, D. Unterleuthner, C. Unger, N. Kramer, M. Hengstschlager, L. Kenner, D. Pfeiffer, G. Krupitza and H. Dolznig, *J. Cell Sci.*, 2017, **130**, 203–218.
- 8 L. Ma, D. Lai, T. Liu, W. Cheng and L. Guo, *Acta Biochim. Biophys. Sin.*, 2010, **42**, 593–602.
- 9 Q. Z. He, X. Z. Luo, K. Wang, Q. Zhou, H. Ao, Y. Yang, S. X. Li, Y. Li, H. T. Zhu and T. Duan, *Cell. Physiol. Biochem.*, 2014, **33**, 173–184.
- 10 G. Francia and R. S. Kerbel, *Nat. Biotechnol.*, 2010, **28**, 561–562.
- 11 J. I. Hare, T. Lammers, M. B. Ashford, S. Puri, G. Storm and S. T. Barry, *Adv. Drug Delivery Rev.*, 2017, **108**, 25–38.
- 12 D. Landesman-Milo and D. Peer, *Bioconjugate Chem.*, 2016, **27**, 855–862.
- 13 G. Francia, S. Man, C. J. Lee, C. R. Lee, P. Xu, M. E. Mossoba, U. Emmenegger, J. A. Medin and R. S. Kerbel, *Clin. Cancer Res.*, 2009, **15**, 6358–6366.
- 14 A. I. Minchinton and I. F. Tannock, *Nat. Rev. Cancer*, 2006, **6**, 583–592.
- 15 M. I. Koukourakis, S. Koukouraki, A. Giatromanolaki, S. C. Archimandritis, J. Skarlatos, K. Beroukas, J. G. Bizakis, G. Retalis, N. Karkavitsas and E. S. Helidonis, *J. Clin. Oncol.*, 1999, **17**, 3512–3521.
- 16 Y. Barenholz, *J. Controlled Release*, 2012, **160**, 117–134.
- 17 Y. Zhang, H. Tang, J. Cai, T. Zhang, J. Guo, D. Feng and Z. Wang, *Cancer Lett.*, 2011, **303**, 47–55.
- 18 D. Sinha, L. Chong, J. George, H. Schluter, S. Monchgesang, S. Mills, J. Li, C. Parish, D. Bowtell, P. Kaur and G. Australian Ovarian Cancer Study, *Clin. Cancer Res.*, 2016, **22**, 1813–1824.
- 19 E. L. LaGory and A. J. Giaccia, *Nat. Cell Biol.*, 2016, **18**, 356–365.
- 20 J. A. Bertout, S. A. Patel and M. C. Simon, *Nat. Rev. Cancer*, 2008, **8**, 967–975.
- 21 M. De Palma, D. Biziato and T. V. Petrova, *Nat. Rev. Cancer*, 2017, **17**, 457–474.
- 22 R. Kalluri and M. Zeisberg, *Nat. Rev. Cancer*, 2006, **6**, 392–401.
- 23 J. M. Hansen, R. L. Coleman and A. K. Sood, *Eur. J. Cancer*, 2016, **56**, 131–143.
- 24 A. Gabizon, H. Shmeeda and Y. Barenholz, *Clin. Pharmacokinet.*, 2003, **42**, 419–436.
- 25 K. M. Laginha, S. Verwoert, G. J. Charrois and T. M. Allen, *Clin. Cancer Res.*, 2005, **11**, 6944–6949.
- 26 D. Peer, J. M. Karp, S. Hong, O. C. Farokhzad, R. Margalit and R. Langer, *Nat. Nanotechnol.*, 2007, **2**, 751–760.
- 27 V. P. Chauhan, T. Stylianopoulos, J. D. Martin, Z. Popovic, O. Chen, W. S. Kamoun, M. G. Bawendi, D. Fukumura and R. K. Jain, *Nat. Nanotechnol.*, 2012, **7**, 383–388.
- 28 D. Rosenblum, N. Joshi, W. Tao, J. M. Karp and D. Peer, *Nat. Commun.*, 2018, **9**, 1410.
- 29 L. Zhang, H. Nishihara and M. R. Kano, *Biol. Pharm. Bull.*, 2012, **35**, 761–766.
- 30 R. K. Jain, *J. Clin. Oncol.*, 2013, **31**, 2205–2218.
- 31 S. M. Tolaney, Y. Boucher, D. G. Duda, J. D. Martin, G. Seano, M. Ancukiewicz, W. T. Barry, S. Goel, J. Lahdenrata, S. J. Isakoff, E. D. Yeh, S. R. Jain, M. Golshan, J. Brock, M. Snuderl, E. P. Winer, I. E. Krop and R. K. Jain, *Proc. Natl. Acad. Sci. U. S. A.*, 2015, **112**, 14325–14330.
- 32 R. K. Jain, *Science*, 2005, **307**, 58–62.
- 33 X. Liu, P. Lin, I. Perrett, J. Lin, Y. P. Liao, C. H. Chang, J. Jiang, N. Wu, T. Donahue, Z. Wainberg, A. E. Nel and H. Meng, *J. Clin. Invest.*, 2017, **127**, 2007–2018.
- 34 H. Shmeeda, S. Even-Chen, R. Honen, R. Cohen, C. Weintraub and Y. Barenholz, *Methods Enzymol.*, 2003, **367**, 272–292.
- 35 X. Wei, D. Shamrakov, S. Nudelman, S. Peretz-Damari, E. Nativ-Roth, O. Regev and Y. Barenholz, *ACS Omega*, 2018, **3**, 2508–2517.
- 36 K. Cohen, R. Emmanuel, E. Kisin-Finfer, D. Shabat and D. Peer, *ACS Nano*, 2014, **8**, 2183–2195.
- 37 D. Peer and R. Margalit, *Neoplasia*, 2004, **6**, 343–353.